

Electronic Supplementary Information

Oxygen Evolution Reaction Electrocatalysis on SrIrO₃ grown using Molecular Beam Epitaxy

Runbang Tang^{1,†}, Yuefeng Nie^{1,2,†}, Jason K. Kawasaki^{2,3,†}, Ding-Yuan Kuo¹,
Guido Petretto⁴, Geoffroy Hautier⁴, Gian-Marco Rignanese⁴,
Kyle M. Shen^{2,3}, Darrell G. Schlom^{1,3} & Jin Suntivich^{1,3,*}

¹ *Department of Materials Science and Engineering,
Cornell University, Ithaca, New York 14853, USA*

² *Laboratory of Atomic and Solid State Physics, Department of Physics,
Cornell University, Ithaca, New York 14853, USA*

³ *Kavli Institute at Cornell for Nanoscale Science,
Cornell University, Ithaca, New York 14853, USA*

⁴ *Institute of Condensed Matter and Nanosciences (IMCN),
Université Catholique de Louvain, Louvain-la-Neuve 1348, Belgium*

* Correspondence: jsuntivich@cornell.edu

† Equal contributions

Experimental Methods

Molecular-Beam Epitaxy (MBE). SrIrO₃ was grown by MBE on single-crystal DyScO₃(110) (CrysTec) using a distilled ozone (O₃) oxidant at the background pressure of 10⁻⁶ Torr. As DyScO₃ has an orthorhombic perovskite structure, to ensure the growth along the SrIrO₃(100)_p direction, we use the (110) orientation of DyScO₃, which is equivalent to the (100) facet in the pseudocubic orientation. Based on the structural data for SrIrO₃¹ and DyScO₃², we estimate ~0.05% compressive strain for the SrIrO₃(100)_p film grown on DyScO₃(110). IrO₂ was grown in a similar fashion on single-crystal TiO₂(110). The epitaxial nature of the as-grown films was confirmed by Reflection high-energy electron diffraction (RHEED, see Figure S1 for SrIrO₃ and Figure S2 for IrO₂) and X-ray diffraction (see Figure S3, XRD, Rigaku). Synchrotron XRD experiments revealed no relaxation of the SrIrO₃ film and the structure retains the same *Pbnm* space group and the rotation pattern (*a*⁻*a*⁻*c*⁺) as bulk SrIrO₃ with the *c* axis (the long axis) oriented in plane with the substrate³.

Electrochemical Characterization. Electrical contacts were made using the same protocol as reported previously^{4, 5}. Briefly, the non-reactive parts of the oxide were covered with a chemically inert epoxy to ensure that only the active surface was exposed to electrolyte. [Fe(CN)₆]^{3-/4-} measurements performed in an Ar-saturated 0.1 M KOH solution with 5 mM K₄Fe(CN)₆·3H₂O (SigmaAldrich, 99.99%) and K₃Fe(CN)₆ (Sigma-Aldrich, 99%) revealed a good ohmic contact (Figure S4). All electrochemical characterization was conducted in a three-electrode glass cell with a potentiostat (Bio-Logic). The reference electrode was a Ag/AgCl redox couple in a saturated KCl solution, calibrated to the H₂ redox in pH 13. The pH dependent experiment was carried out by assuming that RHE shifts by 59 mV per pH using the Nernst equation. The counter electrode was a Pt wire. The electrolyte/cell-resistance-corrected potential

was obtained by correcting the potential with the electrolyte/cell resistance as determined using the high frequency intercept of the real resistance from an impedance measurement. The electrochemical characterizations to assess the cation- and the pH-dependence are shown in Figure S5 and S6.

The OER measurement was conducted in an O₂-saturated KOH solution, prepared from Milli-Q water (18.2 MΩ·cm, Millipore) with KOH pellets (Sigma-Aldrich, 99.995%). Capacitance-free CV curves were obtained by averaging the forward and backward scans. The OER analysis from the CV and the chronoamperometry revealed the same activity (Figure S7). The shaded error bars represent the standard deviations for at least three independent measurements.

All reported electrochemical and OER results are steady-state values. We reach the steady-state results usually by 2nd – 3rd scan. We did not see any change in the electrochemical current after >1 hour of active electrochemical testing. To verify that the steady-scan OER result is truly from the SrIrO₃ surface, we tested the XRD of the SrIrO₃ film after it has reached the steady-state in the OER (more than 10 cycles). The XRD result revealed no observable change (Figure S3). This includes the presence of clear thickness fringes (Kiesig fringes) arising from the SrIrO₃ film with very uniform thickness. Using inductively coupled plasma mass spectrometry (ICP-MS) for the same experiment, we observed Sr²⁺ concentration below the detection limit of the ICP-MS in the electrolyte solution after the OER. Our detection limit corresponds to less an equivalent monolayer of Sr²⁺ assuming the SrIrO₃ film to be perfectly smooth. Therefore, we conclude that the SrIrO₃ film is stable up to the topmost layer, where the stability of the topmost layer is unquantifiable with ICP-MS as there is not enough Sr²⁺ for definite analysis.

DFT calculations. We performed DFT calculations using the projector augmented wave method⁶ as implemented in the Vienna Ab Initio Simulation Package (VASP)⁷. The cutoff on the plane-wave energy is set to 400 eV. The exchange-correlation functional is modeled using the revised Perdew, Burke, and Ernzerhof (PBE) approximation⁸, with the U correction based on a simplified rotationally invariant approach⁹. The surfaces are modeled considering stoichiometric slabs in the orthorhombic perovskite ($Pbnm$)¹⁰ and the tetragonal rutile phases (Figure S8). A vacuum of approximately 13 Å is added to remove the interaction between replicas of the slab. All the calculations include spin-orbit coupling and a dipolar correction along the axis normal to the surface. The surface lattice parameters are fixed to the values obtained from bulk calculations and all the atoms are relaxed until all the forces are smaller than 0.02 eV/Å. The Brillouin zone was sampled using a $6 \times 6 \times 1$ and $4 \times 4 \times 1$ for SrIrO₃ and IrO₂, respectively. The effect of the used U on the band structures and the adsorption energy energies are shown in Figure S9 and S10. The calculation of the free energies shown in Figure 4 includes zero point energy and entropic corrections as reported in the literature¹¹.

RHEED patterns of SrIrO₃ during MBE growth

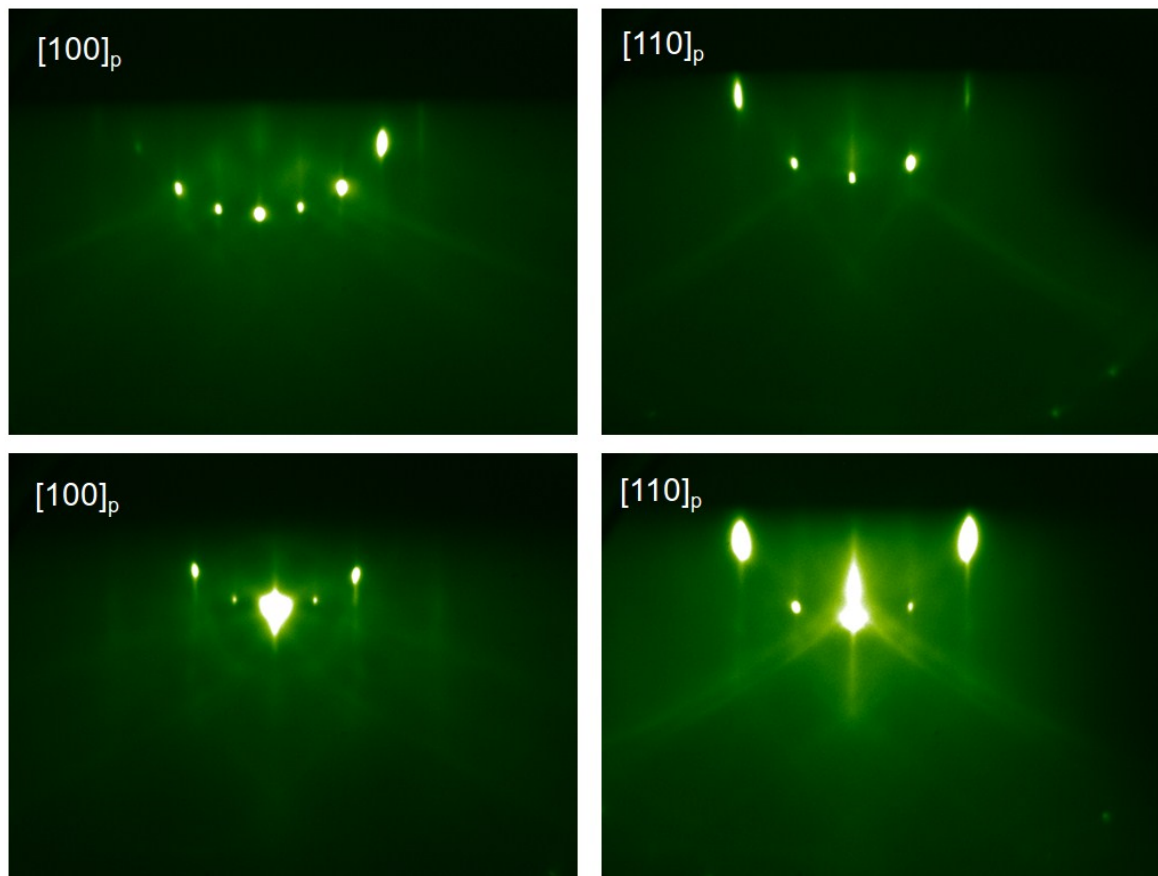


Figure S1. RHEED patterns recorded from SrIrO₃(100)_p/DyScO₃(110). **(Top)** RHEED patterns recorded from a pre-grown DyScO₃ substrate in the equivalent $[100]_p$ and $[110]_p$ azimuth of intended SrIrO₃(100)_p film. **(bottom)** RHEED patterns recorded from SrIrO₃(100)_p/DyScO₃(110) film grown on a DyScO₃ substrate in the equivalent $[100]_p$ and $[110]_p$ azimuth of the SrIrO₃(100)_p film (post-grown).

RHEED patterns of IrO₂ during MBE growth

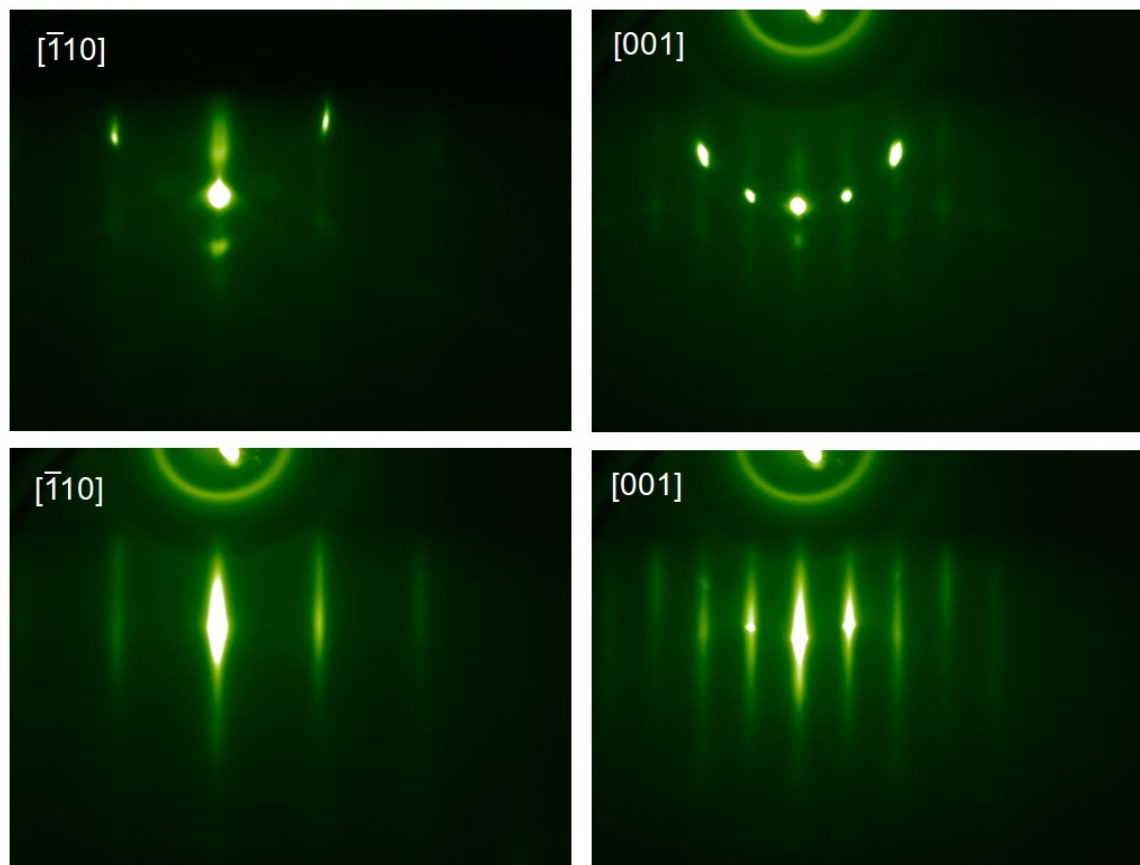


Figure S2. RHEED patterns recorded from IrO₂(110)/TiO₂(110). **(top)** RHEED patterns recorded from a pre-grown TiO₂(110) substrate in the equivalent $[\bar{1}10]$ and $[001]$ azimuth of TiO₂. **(bottom)** RHEED patterns recorded from a IrO₂(110) film grown on a TiO₂(110) substrate in the equivalent $[\bar{1}10]$ and $[001]$ azimuth of the IrO₂(110) film (post-grown).

XRD pattern of SrIrO₃ before and after the OER testing

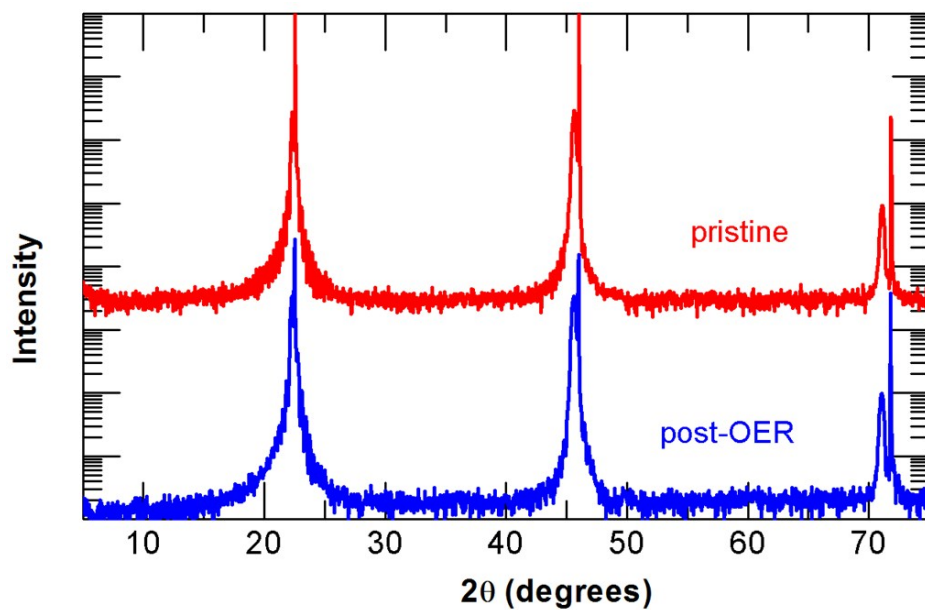


Figure S3. X-ray diffraction (θ - 2θ scan) of the SrIrO₃ film (40 formula-units thick) grown on DyScO₃(110) before and after the OER testing.

CV of SrIrO₃ in the presence of Fe(CN)₆^{3-/4-}

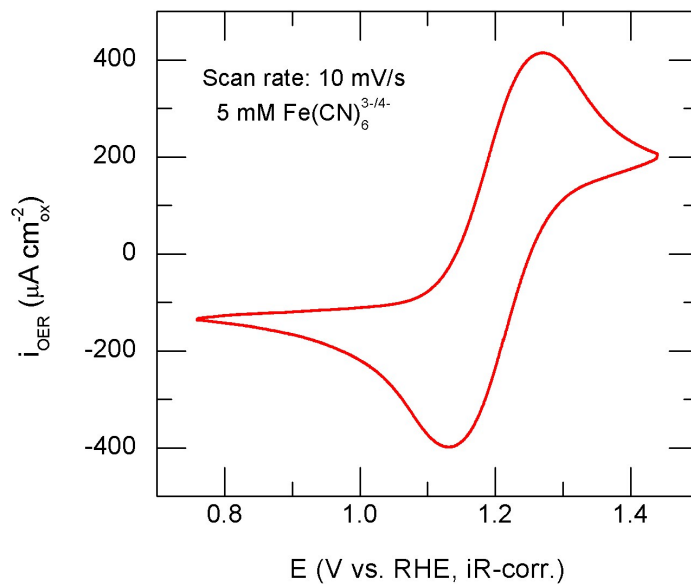


Figure S4. CV of the SrIrO₃ CV in Ar-saturated 0.1 M KOH electrolyte containing 5 mM Fe(CN)₆^{3-/4-} at a 10 mV/s scan rate, illustrating good ohmic contact in the SrIrO₃ film.

The influence of the electrolyte cation on the SrIrO₃ CV

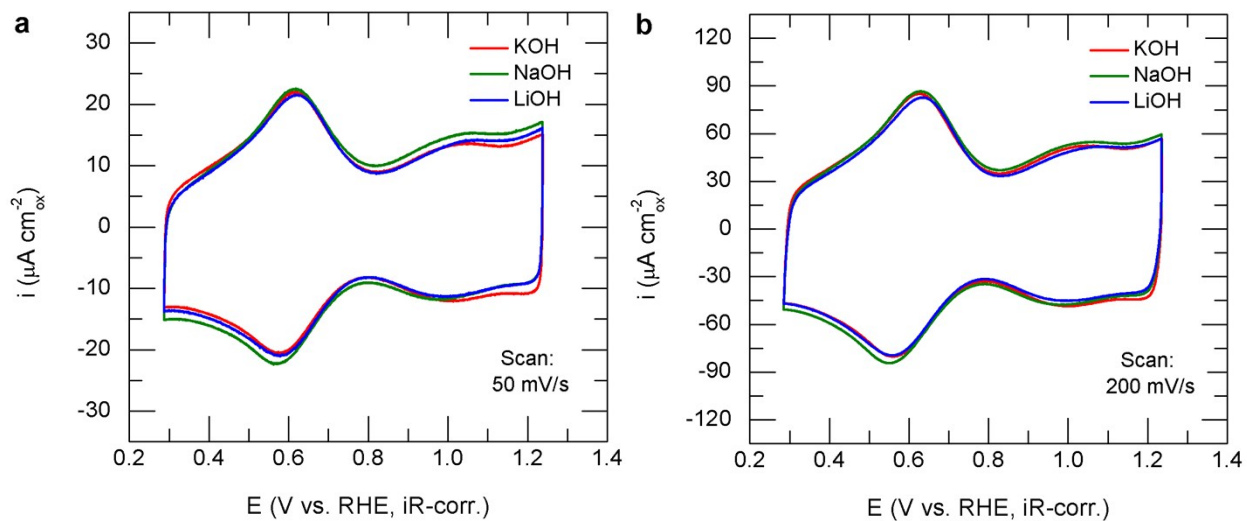


Figure S5. CV of SrIrO₃ in Ar-saturated 0.1M electrolyte of KOH, NaOH, and LiOH at (a) 50 mV/s and (b) 200 mV/s scan rates. We observed no noticeable difference in the CV.

The influence of pH on the SrIrO₃ CV

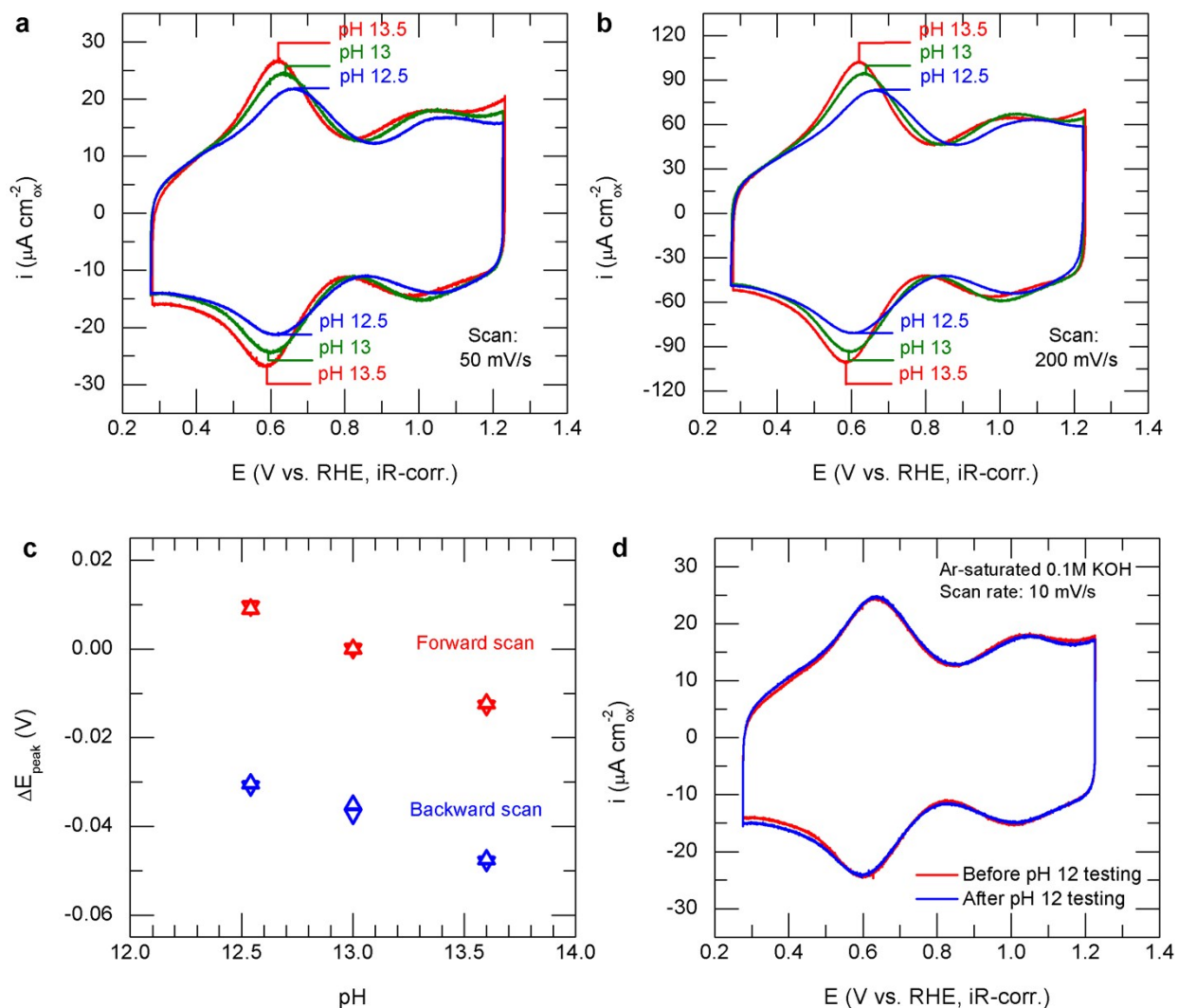


Figure S6. CV of SrIrO₃ in Ar-saturated KOH electrolytes at different pH at the potential scan rate of (a) 50 mV/s and (b) 200 mV/s shows a shift in the redox peak toward higher potential with decreasing pH. As shown in (c) (down-pointing triangle, 50 mV/s scan rate, up-pointing triangle, 200 mV/s scan rate), the shift in the redox peak with pH (with respect to the peak of the forward scan at pH 13) is scan-rate independent. We limit our study to pH > 12 to ensure SrIrO₃ stability. (d) CV of SrIrO₃ in pH 13 before and after an electrochemical test in pH 12, showing SrIrO₃ is stable at pH 12.

Tafel Plot for the OER on SrIrO₃

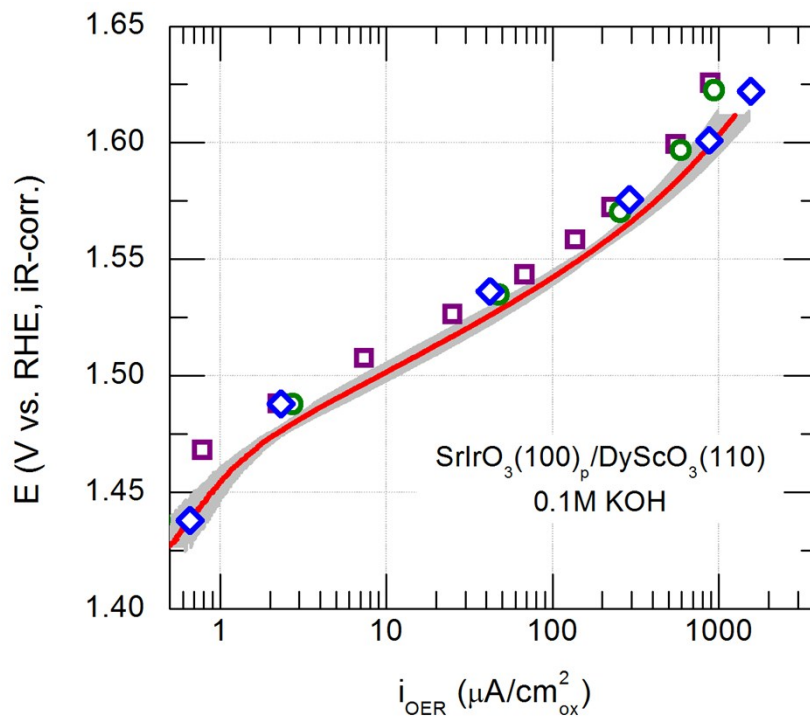


Figure S7. Tafel plot for the OER activities measured via cyclic voltammetry (red line, where the shaded grey region represents the standard deviations from three independent measurements) and chronoamperometry (purple square, green circle, blue diamond, each of which represents independent measurements.)

Relaxed supercells for SrIrO₃ and IrO₂ used for the DFT calculations

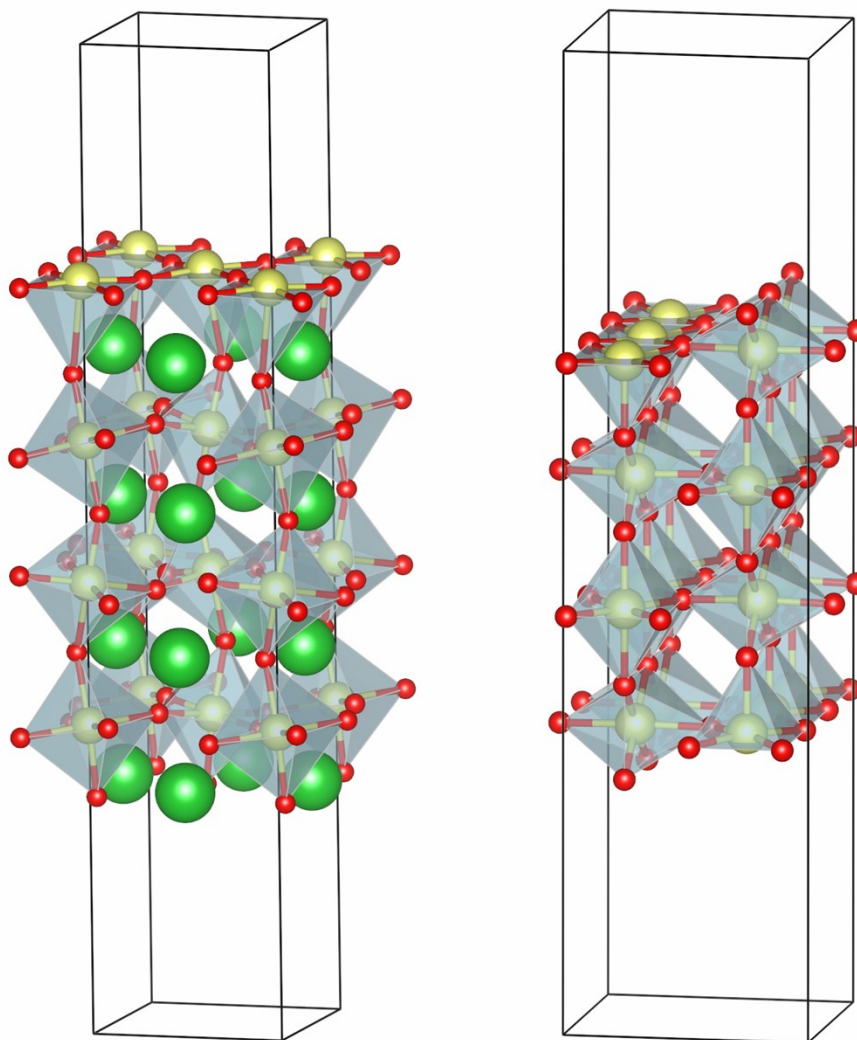


Figure S8. Relaxed supercells for SrIrO₃ (left) and IrO₂ (right). Yellow, red, and green spheres represent Ir, O, and Sr atoms, respectively. In both cases, we have used 4-layer-thick stoichiometric slabs, where we define a layer as a single unit of O-Ir-O along the z -axis. On the IrO₂ surface the bridging O sites are all occupied. Adsorbates placed above the surfaces correspond to 50% coverage.

Calculated band structure of SrIrO₃ for different values of U

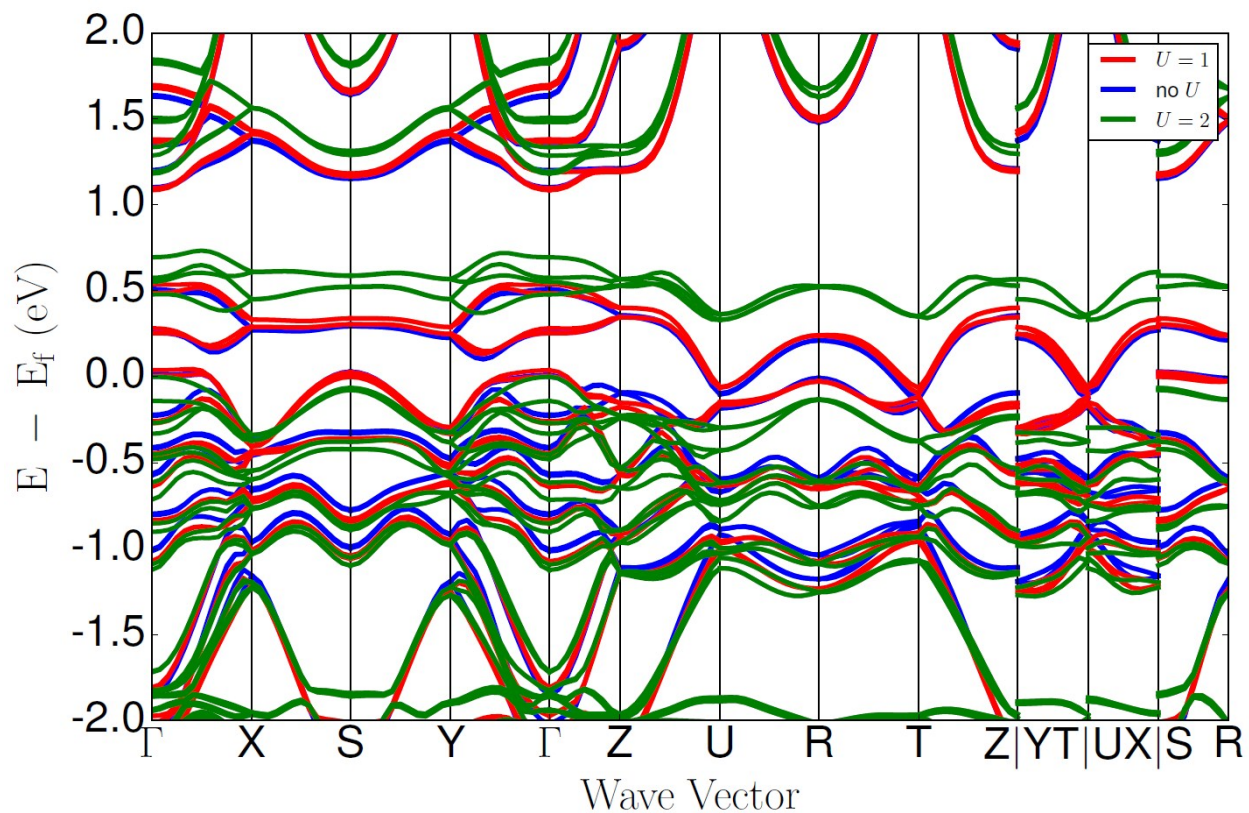


Figure S9. Calculated band structure for SrIrO₃ for different values of U . We point out the opening of the gap for $U = 2$ eV for SrIrO₃, which we put as an upper limit for our DFT calculations.

Adsorption energy shifts on SrIrO₃ and IrO₂ for different values of U

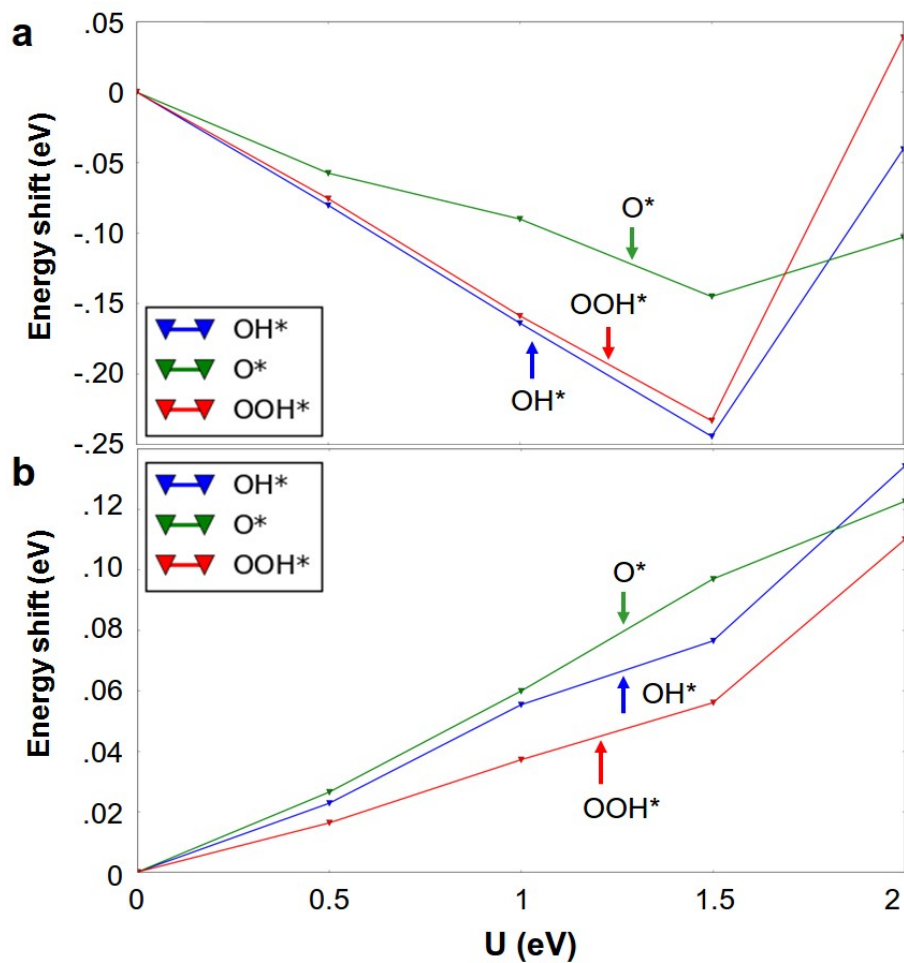


Figure S10. Adsorption energy shifts (OH: blue, O: green, OOH: red) for (a) SrIrO₃(100)_p and (b) IrO₂(110) for different values of U . We point out that the energy shift for SrIrO₃ is greater (~ 0.25 eV) than IrO₂ (~ 0.13 eV).

References

1. J. G. Zhao, L. X. Yang, Y. Yu, F. Y. Li, R. C. Yu, Z. Fang, L. C. Chen and C. Q. Jin, *J. Appl. Phys.*, 2008, **103**, 103706.
2. D. G. Schlom, L. Q. Chen, X. Q. Pan, A. Schmehl and M. A. Zurbuchen, *J. Am. Ceram. Soc.*, 2008, **91**, 2429-2454.
3. Y. F. Nie, P. D. C. King, C. H. Kim, M. Uchida, H. I. Wei, B. D. Faeth, J. P. Ruf, J. P. C. Ruff, L. Xie, X. Pan, C. J. Fennie, D. G. Schlom and K. M. Shen, *Phys. Rev. Lett.*, 2015, **114**, 016401.
4. K. A. Stoerzinger, L. Qiao, M. D. Biegalski and Y. Shao-Horn, *J Phys Chem Lett*, 2014, **5**, 1636-1641.
5. K. A. Stoerzinger, M. Risch, J. Suntivich, W. M. Lu, J. Zhou, M. D. Biegalski, H. M. Christen, Ariando, T. Venkatesan and Y. Shao-Horn, *Energy Environ. Sci.*, 2013, **6**, 1582-1588.
6. P. E. Blochl, *Phys. Rev. B*, 1994, **50**, 17953-17979.
7. G. Kresse and J. Furthmuller, *Phys. Rev. B*, 1996, **54**, 11169-11186.
8. B. Hammer, L. B. Hansen and J. K. Norskov, *Phys. Rev. B*, 1999, **59**, 7413-7421.
9. S. L. Dudarev, G. A. Botton, S. Y. Savrasov, C. J. Humphreys and A. P. Sutton, *Phys. Rev. B*, 1998, **57**, 1505-1509.
10. Y. L. Lee, J. Kleis, J. Rossmeisl and D. Morgan, *Phys. Rev. B*, 2009, **80**, 224101.
11. I. C. Man, H. Y. Su, F. Calle-Vallejo, H. A. Hansen, J. I. Martinez, N. G. Inoglu, J. Kitchin, T. F. Jaramillo, J. K. Norskov and J. Rossmeisl, *ChemCatChem*, 2011, **3**, 1159–1165.